



CHALMERS
UNIVERSITY OF TECHNOLOGY

Performance of iron sand as an oxygen carrier at high reduction degrees and its potential use for chemical looping gasification

Downloaded from: <https://research.chalmers.se>, 2024-04-24 19:24 UTC

Citation for the original published paper (version of record):

Purnomo, V., Stanicic, I., Mei, D. et al (2023). Performance of iron sand as an oxygen carrier at high reduction degrees and its potential use for chemical looping gasification. Fuel, 339. <http://dx.doi.org/10.1016/j.fuel.2022.127310>

N.B. When citing this work, cite the original published paper.



Full Length Article

Performance of iron sand as an oxygen carrier at high reduction degrees and its potential use for chemical looping gasification

Victor Purnomo^{a,*}, Ivana Staničić^b, Daofeng Mei^b, Amir H. Soleimanisalim^b, Tobias Mattisson^b, Magnus Rydén^b, Henrik Leion^a

^a Division of Energy and Materials, Department of Chemistry and Chemical Engineering, Chalmers University of Technology, Göteborg 412 58, Sweden

^b Division of Energy Technology, Department of Space, Earth, and Environment, Chalmers University of Technology, Göteborg 412 58, Sweden

ARTICLE INFO

Keywords:

Iron sand
Oxygen carrier
Chemical looping gasification
High reduction degree
Fluidized bed
Thermodynamics

ABSTRACT

Iron sand as an industrial by-product has a reasonable iron content (35 wt% Fe) and low economical cost. The reactivity of iron sand as an oxygen carrier was examined in a bubbling fluidized bed reactor using both gaseous and solid fuels at 850–975 °C. Pre-reductions of iron sand were performed prior to fuel conversion to adapt the less-oxygen-requiring environment in chemical looping gasification (CLG). Based on the investigations using CO and CH₄, iron sand has an oxygen transfer capacity of around 1 wt%, which is lower than that of ilmenite. The conversion of pine forest residue char to CO and H₂ was higher when using iron sand compared to ilmenite. Depending on the mass conversion degree of iron sand, the activation energy of pine forest residue char conversion using iron sand was between 187 and 234 kJ/mol, which is slightly lower than that of ilmenite. Neither agglomeration nor defluidization of an iron sand bed occurred even at high reduction degrees. These suggests that iron sand can be utilized as an oxygen carrier in CLG. Furthermore, this study presents novel findings in the crystalline phase transformation of iron sand at various degrees of oxidation, altogether with relevant thermodynamic stable phases.

1. Introduction

The chemical-looping technology is a promising alternative for biomass-based energy conversion and can also achieve a negative CO₂ emission. A chemical-looping process is comprised of two reactors, air and fuel reactors, where an oxygen carrier is circulated to be oxidized and reduced using air and fuel in the respective reactor. A fuel is fed into the fuel reactor and reacts with oxygen that is carried by the oxygen carrier (OC). When solid fuel is used, either steam or CO₂ is also fed to the fuel reactor as a fluidizing gas, which facilitates the conversion of the char fraction of the fuel. In this way, the formed flue gases, mainly comprised of carbon dioxide and steam, are expected to exit the fuel reactor without being mixed with nitrogen. This is a clear advantage since nitrogen causes a significant decrease in the heating value of the generated flue gases from the fuel conversion [1]. Moreover, the capture of the carbon dioxide can hence be easily achieved through a simple condensation of steam, thus eliminating the need for an additional gas separation unit.

Among the known chemical looping processes, chemical looping

gasification (CLG) currently emerges as a way to obtain high-quality syngas with the possibility to significantly reduce the emission of CO₂. If biomasses are used as fuel, this can even lead to a possibility of a negative CO₂ emission, which means removal of CO₂ content in the atmosphere [2]. Contrary to the commonly known chemical looping combustion (CLC), the oxygen transfer from the air reactor (AR) to the fuel reactor (FR) in a CLG unit needs to be controlled so that fuel conversion to CO and H₂ can be maximized. This can consequently cause a partial oxidation of the OC, which may lead to a further reduction of OC in the FR compared to that in a CLC unit. A schematic diagram of CLG is illustrated in Fig. 1 [3].

An oxygen carrier plays an important role in chemical looping processes [4]. A good oxygen carrier is expected to have the following properties: environmentally sound, good fluidization performance, sufficiently durable, and highly reactive [5]. It is also preferred that the oxygen carrier is economically cheap and abundantly available [6]. The viability of different oxygen carriers has been studied extensively in the past decades, with the most common being nickel, copper, manganese, and iron-based materials [7]. Among them, previous studies have stated that iron-based oxygen carriers are abundantly available, relatively

* Corresponding author.

E-mail address: purnomo@chalmers.se (V. Purnomo).

<https://doi.org/10.1016/j.fuel.2022.127310>

Received 19 July 2022; Received in revised form 23 November 2022; Accepted 25 December 2022

Available online 5 January 2023

0016-2361/© 2023 The Authors. Published by Elsevier Ltd. This is an open access article under the CC BY license (<http://creativecommons.org/licenses/by/4.0/>).

Nomenclature

AR	Air reactor
AHA	Associative hydrogen adsorption
BET	Brunauer-Emmett-Teller
CLC	Chemical looping combustion
CLG	Chemical looping gasification
CLOU	Chemical looping oxygen uncoupling
CLR	Chemical looping reforming
DHA	Dissociative hydrogen adsorption
E_a	activation energy (kJ/mol)
EDX	Energy dispersive X-ray analysis
FR	Fuel reactor
LHHW	Langmuir-Hinshelwood/Hougen-Watson
k	rate constant (s^{-1})
M_i	molecular weight of element i (gram/mole)
m_{ox}	mass of a fully oxidized sample (gram)

\dot{n}	gas molar flow (mole/second)
OC	Oxygen carrier
OE	Oxygen exchange
p_{H_2}	Hydrogen partial pressure (atm)
r	conversion rate of pine forest residue char (s^{-1})
r_i	conversion rate of gaseous fuel i (s^{-1})
R_o	oxygen transfer capacity (%)
SEM	Scanning electron microscopy
t	time (second)
TGA	Thermogravimetric analysis
X_c	fraction of char conversion
XRD	X-ray diffraction
x_i	molar fraction of species i
ω	mass conversion degree
ω_{red}	mass conversion degree when no more fuel conversion products can be observed in the outlet

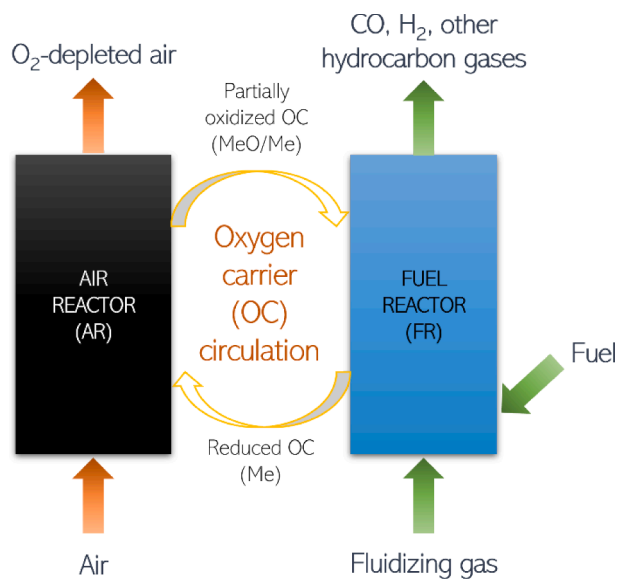


Fig. 1. A schematic diagram of chemical looping gasification (CLG). Limited oxygen transfer from the AR to the FR may result in a partially oxidized OC and, hence, a higher reduction of the OC in the FR compared to that in chemical looping combustion (CLC).

inexpensive and environmentally friendly. Sirkawar et al. [8] stated that Fe_2O_3 is a preferred metal oxide to be used as an oxygen carrier since it fulfills many of the aforementioned oxygen carrier properties. Yu et al. [9] provided a broad review of iron-based oxygen carriers in chemical looping technology and emphasized that the reactivity and mechanical stability are the most important factors to consider in selecting oxygen carriers. Matzen et al. [10] pointed out that materials based on natural ores, including iron ores, are attractive due to their inexpensive cost. Specifically for chemical looping application, ilmenite is generally recognized as a benchmark oxygen carrier since it fulfills all the aforementioned oxygen carrier criteria [11].

Nevertheless, an interest of using a waste-based, instead of an ore-based, material is currently emerging to support a circular economy [12]. With respect to this, the use of by-product-based oxygen carrier can reduce both waste generation and the required cost to run a power plant [13]. Qasim et al. [5] suggested that the utilization of waste-based materials can be useful to tackle the emerging environmental issues. Several studies have, for example, investigated the use of red mud, a by-

product of alumina production from bauxite, as an oxygen carrier [14–16]. One review article by Störner et al. [17] listed iron sand produced by Boliden AB in Northern Sweden as a by-product-based bed material alternative. Despite being abundantly available globally [18], iron sand, also known as copper slag, as an oxygen carrier was only previously studied in a fixed bed setup [19–22]. It is important to note that no previous studies have examined the performance of iron sand as an oxygen carrier in a chemical looping gasification (CLG) unit or in a fluidized bed setup using a biomass char, let alone at high reduction degrees where the risk for agglomeration or defluidization is present [23]. Seen from these perspectives, iron sand is an attractive oxygen carrier material to investigate, especially for CLG application.

The aim of this study is to better understand the performance of iron sand by investigating the reactivity and oxygen carrier capacity at different reduction degrees relevant for chemical looping. The performance has been investigated in a bubbling fluidized batch reactor where high reduction degrees were obtained through the pre-reduction of iron sand. In CLG, the oxygen transfer from AR to FR is controlled by the circulation rate which sets the reduction degree of the oxygen carrier [19]. Here, the pre-reduction of iron sand in the batch fluidized bed reactor setup allows controlling the reduction degree. The study was performed by investigating: i) the reactivity and oxygen transfer capacity of iron sand with two gaseous fuels, CO and CH_4 , and ii) the kinetics and hydrogen inhibition effect on the conversation rate of one biomass-based solid fuel, pine forest residue char. Iron sand was characterized using Scanning Electron Microscopy/Energy-Dispersive X-ray (SEM/EDX) to examine the physical properties and X-ray diffraction (XRD) to study the crystalline phases. Lastly, FactSage 8.1 with relevant databases was used to predict the phase transformations occurring during biomass conversion and verified by comparison with crystalline phases obtained by X-ray diffraction (XRD).

2. Materials and methods

2.1. Fluidized bed batch reactor setup

All experiments were conducted in a fluidized bed batch reactor. The setup was able to feed oxidizing and reducing gases alternatively into the reactor, representing AR and FR in a chemical-looping system. Inert gas was introduced to the reactor in between the oxidizing and reducing periods to prevent gas mixing. The schematic setup of the experimental equipment is illustrated in Fig. 2.

The feeding of gases was regulated by three magnetic valves as shown in Fig. 2. Solid fuel was fed into the reactor from the top, while either steam or gaseous fuel was fed through the bottom during the

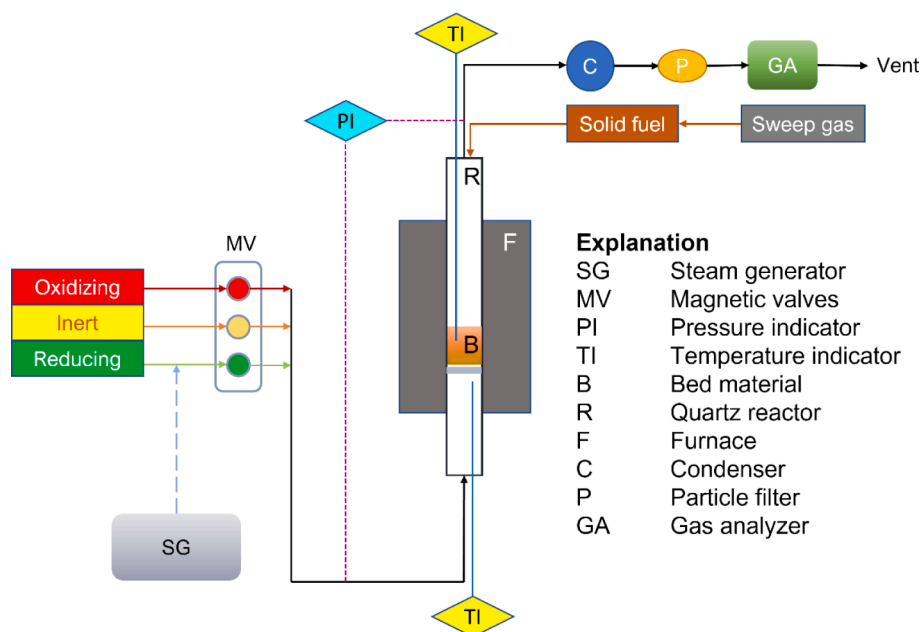


Fig. 2. A schematic setup of the fluidized bed batch reactor system.

reduction phase. The height and inner diameter of the quartz glass reactor were 820 mm and 22 mm, respectively. The bed particles were placed on top of a porous circle-shaped quartz plate, which was located 370 mm above the reactor's bottom edge. The reactor was placed in a high-temperature furnace manufactured by ElectroHeat Sweden AB. The up-and-downparts of the reactor were equipped with tightly sealed connections to avoid gas leakage. To avoid gas condensation downstream of the reactor, which can affect the gas measurement, heating tape was wrapped around the top of the reactor. In the experiments with solid fuel, additional heating tape was installed around the bottom of the reactor to avoid steam condensation. Sweep gas was introduced from the top of the reactor to assist the feeding of solid fuels. The temperature inside the bed of particles was measured using a type-K thermocouple that was placed in a quartz cover. The outlet gases were cooled down by an M&C ECP1000 condenser, which can work with a gas flow of 150 l/h or below with a total cooling capacity of 50 kJ/h at room temperature (25 °C), so that no steam enters the analyzer. A Rosemount™ NGA 2000 gas analyzer measured the real-time gas volumetric flow rates and concentration using a non-dispersive infrared (NDIR) analyzer module with a repeatability of around 1 % and a minimum detection capacity of around 100 ppm, except for O₂ which is around 0.1 %. The calibration ranges of the gas analyzer were from 0 % to 25 %, 20 %, 15 %, 40 %, and 5 % for CH₄, CO, H₂, CO₂, and O₂, respectively. The gas analyzer can measure a gas flow between 500 and 1400 ml/min at a temperature between 0 and 55 °C at a pressure of 690 hPa-gauge or below with a maximum power of 100 W. The steam was generated at 150 °C by the controlled evaporator mixer Bronkhorst type W-202A-300-K that can work with a maximum temperature of 200 °C. To monitor the fluidization of the bed particle, a 20-Hz Honeywell pressure transducer was employed to measure the pressure difference between the inlet and outlet of the reactor. The frequency of 20 Hz was deemed sufficient to judge the fluidization state of the bed based on the pressure fluctuations caused by the fluidized bed itself [3]. The setup design has been reported previously [24].

2.2. Oxygen carrier

Iron sand was first calcined in air in a high-temperature furnace at 950 °C for 12 h to improve its reactivity and mechanical strength [25]. The calcined oxygen carrier was then sieved to the size range 125 – 180

μm and subsequently activated at 850 °C for a minimum of 4 redox cycles in the fluidized bed batch reactor prior to any investigations to ensure the fuel conversion stability [26]. The main composition of the iron sand was provided by Boliden AB and can be seen in Table 1. It should be noted that oxygen content was excluded here, thus the total mass does not add up to 100 wt%. The bulk density of iron sand was around 1,286 kg/m³. This corresponds to approximately 40-, 30-, and 27-mm-high beds, respectively, in the current reactor at static conditions. The used particles were exposed to at least 60 cycles of oxidation – reduction, excluding the activation step, in the fluidized batch reactor. A BET surface analysis using nitrogen at 77 K showed that the pore area of fresh calcined and used iron sand were 0.049 and 0.997 m²/g, respectively.

2.3. Investigations of oxygen transfer capacity and reactivity of iron sand using gaseous fuels

Methane and carbon monoxide were used as gaseous fuels to investigate both oxygen transfer capacity and reactivity of iron sand in the fluidized bed batch reactor. The reason for using these gases is because they make up part of gaseous substances released from the conversion of solid fuels, e.g., biomasses.

15 g of oxygen carrier bed was put in the quartz reactor, which was then heated up in a furnace to a desired reaction temperature, which was either 850, 875, 900, 950 or 975 °C. At the same time, the oxygen carrier became fully oxidized during the heating, see the oxidation step in Table 2. The oxygen carrier bed for the methane experiment consists of 100 % iron sand, while that for the CO experiment comprised 5 g iron sand and 10 g quartz sand. Mixing iron sand with quartz sand in the latter case was done to slow down the conversion of CO, which is expected to be quick due to the high reactivity of iron sand toward CO. In order to obtain iron sand at different mass conversion degrees, i.e., oxidation states, prior to the conversion of either methane or carbon monoxide, iron sand was primarily reduced using syngas (50/50, CO/H₂) for certain durations. Different mass conversion degree of the oxygen carrier implies different reactivity of oxygen carrier. The gaseous fuel, either methane or carbon monoxide, was then injected into the oxygen carrier bed in 10 pulses of 4-second injection. The inert gas was injected for a short duration of 60 s between each pulse. Pulsing was performed to minimize the effect of gas back mixing [3], which may

Table 1

The main composition of iron sand used in this work, in weight percentage (wt %).

Fe	Si	Al	Ca	Mg	Zn	Cu	Na	K	Mn	S	Ba	Cr	Sn	Mo	Ti
35	16	2.4	2.3	1.3	1.2	0.83	0.46	0.40	0.35	0.24	0.20	0.19	0.18	0.17	0.13

Table 2

The procedure of a cycle in the investigations using gaseous fuels.

Step	Duration (s)	Gases	Flow rate
Oxidation	Until OC is fully oxidized	5 % O ₂ in N ₂	1000 ml/min
Inert	180	Pure N ₂	1000 ml/min
Pre-reduction using syngas	0 – 60	50 % CO and 50 % H ₂	450 ml/min*
Inert	180	Pure N ₂	1000 ml/min
Gaseous fuel conversion	10 pulses of 4-s injection, with a 60-s inert in between	Pure CH ₄ or pure CO	450 ml/min
Inert	180	Pure N ₂	1000 ml/min

*For the experiment using methane as the fuel at 900 °C, the syngas flow was set to 600 ml/min due to the use of a different gas flow regulator.

occur within the system, particularly in the setup between the reactor and the gas analyzer. This phenomenon may interfere with the determination of the intrinsic reactivity of iron sand, which is the main purpose of this investigation. The complete procedure in a cycle is shown in Table 2. Temperatures above 850 °C are typically used in chemical looping gasification, especially in the fuel reactor [27]. The fluidization was monitored throughout the whole experiment using pressured drop measurements as described above. Depending on the temperature and the fluidizing gas, the superficial velocity of the bed was between 7 and 18 cm/s, while the minimum fluidization velocity was about 0.4 cm/s based on Wen and Yu's correlation. Despite being relatively high compared to the minimum fluidization velocity, the superficial velocity was still well below the terminal velocity, which is in a range between 26 and 34 cm/s. Hence, the fluidization regime is bubbling.

2.4. Conversion of solid fuel

The conversion of forest residue char was investigated using iron sand as an oxygen carrier. The raw pine forest residue was converted to char through devolatilization at 950 °C for 2 min in an inert atmosphere and then sieved and crushed to the size range 125 – 500 µm. This was performed to remove most of the volatile contents in the biomass as it would likely interfere with the char conversion evaluation, which was the main ambition with this investigation. The volatile contents of the raw pine forest residue make up around 80 wt% of the fuel content. The fuel content after the devolatilization is presented in Table 3. The

Table 3

The content of pine forest residue char, in weight percentage (wt%).

Proximate analysis	
Total moisture	5.3
Ash	14
Ultimate analysis of ash, dry basis	
C	79
H	0.50
N	0.47
S	0.06
Cl	0.01
O, by subtraction	5.0
Ash	15
HHV (MJ/kg)	27

moisture content in the devolatilized char was caused by moisture absorption during the storing of char for months prior to the analysis.

Similar to the experiments using gaseous fuels, oxygen carrier was first fully oxidized during heating up to a desired reaction temperature, i.e., either 850, 900, 950, or 975 °C. A trace amount of less than 0.1 mg SO₂ per gram iron sand was released during the oxidation, which is likely due to the sulfur content within the iron sand itself. Prior to the solid fuel conversion, iron sand was pre-reduced using diluted CO for certain durations, see Table 4, to obtain different mass conversion degrees of iron sand. Here, CO was used instead of syngas due to a technical reason. In principle, any reducing gas can be used for a pre-reduction as long as the gas can be converted easily. Afterward, steam was fed to the oxygen carrier bed for 2 min and char particles were fed in batches into the oxygen carrier bed with assistance of a sweep gas, see Table 4. The steam was generated at 150 °C. Depending on the temperature, the superficial velocity of the bed during the experiments was between 10 and 11 cm/s, with a minimum fluidization velocity of about 0.4 cm/s based on Wen and Yu's correlation. As explained in section 2.3, the superficial velocity is still below the terminal velocity (26 – 34 cm/s) and thus indicates a bubbling regime of the fluidized bed.

The complete procedure in a cycle is summarized in Table 4. Every oxidation – reduction cycle has been repeated three times. The total number of cycles iron sand has been exposed to during the solid fuel experiment was 60 cycles.

2.5. Data evaluation

The mass conversion of the oxygen carrier, ω , during reduction with carbon monoxide [28], syngas [29], and methane [29] was calculated based on Equation (1) – (3), respectively, based on the composition in the outlet gas. The accuracy of mass conversion degree may vary depending on the fluidizing gas and the conversion level. A lower mass conversion degree usually implies a higher deviation. Nevertheless, the statistical variation is still deemed acceptable since it is not substantial enough to cause a wrong interpretation in important analysis, e.g., crystalline phases transformation and reactivity determination.

$$\omega_{CO} = 1 - \int_{t_0}^t \frac{\dot{n}M_O}{m_{ox}} (x_{CO_2}) dt \quad (1)$$

Table 4

The procedure of a cycle in the solid fuel experiments.

Step	Duration (s)	Materials and gases	Flow rate
Oxidation	Until OC is fully oxidized	5 % O ₂ in N ₂	600 ml/min
Inert	180	Pure N ₂	600 ml/min
Pre-reduction using CO	0, 50, 100, 150, 200	50 % CO in N ₂	600 ml/min
Inert	180	Pure N ₂	600 ml/min
Solid fuel gasification	Until no more carbon conversion was observed	Solid fuel: pine forest residue char Sweep gas: pure N ₂	0.1 g/cycle 300 ml/min
		Fluidizing gas: 50 % steam in N ₂	600 ml/min
Inert	180	Pure N ₂	600 ml/min

$$\omega_{\text{syngas}} = 1 - \int_{t_0}^t \frac{\dot{n}M_O}{m_{\text{ox}}} (2x_{\text{CO}_2} + x_{\text{CO}} - x_{\text{H}_2}) dt \quad (2)$$

$$\omega_{\text{CH}_4} = 1 - \int_{t_0}^t \frac{\dot{n}M_O}{m_{\text{ox}}} (4x_{\text{CO}_2} + 3x_{\text{CO}} - x_{\text{H}_2}) dt \quad (3)$$

The oxygen transfer capacity of iron sand, R_o , can be calculated in the same way as ilmenite [11]. Here, R_o can be assumed as the difference between the mass conversion degree when iron sand was fully oxidized, i.e., $\omega = 100\%$, with that when only unconverted fuel was found in the outlet, which is assigned as ω_{red} . The latter implies that the available oxygen in iron sand was already exhausted completely. Note that there might still be oxygen left in the material, for example the oxygen associated to phases like SiO_2 , but this oxygen is not available for reaction due to possible thermodynamic or, to a greater extent, kinetic limitations. In this study, R_o can be obtained with respect to fuel i , either CO or CH_4 .

$$R_{O,i} = 100\% - \omega_{\text{red}} \quad (4)$$

The reactivity of gaseous fuel i , either methane or carbon monoxide, that was pulsed into the reactor was defined as the change of mass conversion degree over time and calculated for every pulse according to Equation (5). For graphing purposes, an average of mass conversion degrees in a pulse was taken as the representing mass conversion degree.

$$r_i = \frac{-d\omega}{dt} \quad (5)$$

For the solid fuel experiment, the fraction of char conversion, X_c , was defined as the ratio of the total carbon released at a specific time to the total carbon emitted from the converted char, $m_{c,\text{total}}$ [28], during a cycle in the char conversion. This can be seen in Equation (6).

$$X_c = \frac{M_c \int_{t_0}^t \dot{n}(t) (X_{\text{CO}}(t) + x_{\text{CO}_2}(t) + x_{\text{CH}_4}(t)) dt}{m_{c,\text{total}}} \quad (6)$$

The conversion rate of solid fuel r was calculated according to Equation (7).

$$r = \frac{dX_c}{(1 - X_c)dt} \quad (7)$$

In this work, the mean of the conversion rate was calculated over the char conversion interval of 0.3 to 0.7, as this range was deemed as giving a good view of the char reactivity, something which has also been seen in previous works in the same setup [30]. This also applies to the other related parameters, such as hydrogen partial pressure and $(\frac{\text{CO}}{\text{CO} + \text{CO}_2})$ ratio.

The partial pressure of hydrogen was defined as the arithmetic average between that of the inlet and outlet over the three repeated cycles [31].

$$pH_2 = \frac{pH_{2,\text{inlet}} + pH_{2,\text{outlet}}}{2} \quad (8)$$

The ratio of CH_4 to the sum of CH_4 , CO, and CO_2 ($\frac{\text{CH}_4}{\text{CH}_4 + \text{CO} + \text{CO}_2}$) and the ratio of CO to the sum of CO and CO_2 ($\frac{\text{CO}}{\text{CO} + \text{CO}_2}$) was calculated as the average of the three repeated cycles.

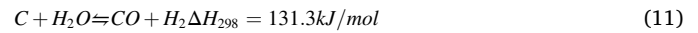
2.6. Char reactivity models

The Arrhenius formula, as shown in Equation (9), was used to obtain the kinetic parameters of char conversion toward iron sand. Here, the char conversion rate is given as a function of temperature. The equation can be derived to Equation (10), which can be the basis for plotting the reaction rate r as a function of temperature T to obtain the kinetic rate constant, k , and activation energy, E_a .

$$r = ke^{-\frac{E_a}{RT}} \quad (9)$$

$$\ln(r) = \ln(k) - \frac{E_a}{RT} \quad (10)$$

Char conversion can be limited by the presence of H_2 and CO [32,33], where the former is the one that greatly suppresses the steam conversion of solid fuels [34]. Therefore, only the H_2 inhibition effect was considered in this work since steam was used as the gasifying agent during the char conversion, i.e., the CO inhibition effect is negligible [30]. Since the size of the fuel particles was limited to between 125 and 500 μm , which is relatively small, the effect of the diffusion of oxygen was not taken into account in this study [35]. Langmuir-Hinshelwood/Hougen-Watson (LHHW) models were used to interpret the conversion mechanism in this work since the models are applicable to describe char conversion in a mixture of steam, CO_2 , H_2 , and CO, which is the case in this study [34]. The main reaction [36] is



Based on the LHHW mechanism, the conversion rate can be expressed according to either oxygen exchange (OE), associative hydrogen adsorption (AHA) or dissociative hydrogen adsorption (DHA) models, all based on the surface reactions between the char and the surrounding gas environments. Table 5 summarizes the models with their respective surface reactions [30]. In the table, C(X)_n is a surface complex formed by a carbon molecule and n molecules of species X , while C_f is a free-active site of carbon.

The OE and AHA models have the same reaction order and therefore share the same rate expression, which can be seen in Equation (12), while the DHA model is expressed as Equation (13). Both models have conversion rates expressed as functions of hydrogen partial pressure. It should be noted that steam partial pressure in the bed was assumed constant during the experiment, i.e., $p_{\text{H}_2\text{O}} = 0.5$, and therefore is not considered as a variable in the rate expressions.

$$\text{OE/AHA: } r = \frac{1}{a + b p_{\text{H}_2}} \quad (12).$$

$$\text{DHA: } r = \frac{1}{a + b \sqrt{p_{\text{H}_2}}} \quad (13).$$

Here, a and b represent several temperature-dependent kinetic parameters that are based on the presented surface reactions that may take place during the char conversion. Since it is rather difficult to determine the kinetic parameters due to the constant steam partial pressure, only a and b are used in this study. Hence, a and b are also influenced by the gas phase concentrations. A detailed elaboration of what a and b stand for has previously been presented [30].

2.7. Characterization and thermodynamic calculations

The phases of fully oxidized and several reduced iron sand samples from a separate experiment were analyzed using XRD Bruker D8. Specifically for this purpose of characterization, iron sand was exposed to 450 ml/min pure CO at 850 °C and reduced to different mass conversion degrees. The surface morphology and elemental distribution in the iron sand samples were analyzed using SEM/EDX JEOL 7800F Prime using backscattered electron detector. The iron sand particles were embedded

Table 5
Three LHHW-based models to predict the char conversion mechanism.

Models	Surface reactions	Explanation
Oxygen exchange (OE)	$\text{C(O)} + \text{H}_2 \rightarrow \text{C}_f + \text{H}_2\text{O}$	The reverse reaction of C(O) complex formation, which is a result from the reaction between C_f and steam
Associative hydrogen adsorption (AHA)	$\text{C}_f + \text{H}_2 \rightleftharpoons \text{C(H)}_2$	The hydrogen inhibition mechanism which forms C(H)_2 complex
Dissociative hydrogen adsorption (DHA)	$\text{C}_f + 0.5\text{H}_2 \rightleftharpoons \text{C(H)}$	The hydrogen inhibition mechanism which forms C(H) complex

in epoxy to provide cross-sectional view under this analysis. The BET surface area analysis was performed using Micromeritics TriStar 3000.

The thermodynamic equilibrium calculation was conducted using FactSage 8.1 [37]. The module Phase Diagram was utilized along with the major components of iron sand, Fe and Si, according to the composition reported in Table 1. Temperatures between 800 and 1,000 °C were investigated with different reduction potentials to simulate the experiments in this study. Stoichiometric solids from the databases FactPS and FToxid were selected along with the solution phases spinel, clinopyroxene, monoxide and slag.

3. Results and discussion

3.1. Investigations of oxygen capacity and reactivity of iron sand using gaseous fuels

The oxygen capacity and reactivity of iron sand toward methane and carbon monoxide was examined at four temperatures and four mass conversion degrees. Iron sand was first reduced with syngas to set the mass conversion degree, then 10 pulses of the respective gaseous fuel were subsequently injected into the reactor. The pulsing of gaseous fuels is the basis for the kinetic study conducted in this work. Fig. 3 illustrates the concentration profiles of a 30-second syngas injection followed by the pulsing of a gaseous fuel, which is methane in this case. The alternating height of the methane peaks was caused by artefacts in the gas analyzer, which often happened at high reduction degrees. However, this was deemed as a small noise which did not disturb the reactivity determination substantially.

3.1.1. Investigations using methane

Iron sand was first reduced with syngas to set its mass conversion degree before reacting with methane. Pulsing was performed so that a change in reactivity could be demonstrated in a more discreet way, thus ruling out the back mixing effect that is present in a continuous experiment [3]. Fully oxidized iron sand was also examined with methane pulses. Mass conversion degree of iron sand after pre-reduction using syngas can be seen in Table S.1. The volumetric flow of syngas was 450 ml/min, except for the investigations at 900 °C, in which syngas was

600 ml/min, see Table 2.

Ten pulses of methane were subsequently fed into the particle bed after syngas injection. The reactivity of iron sand toward methane in every pulse was calculated according to Equation (5). Fig. 4 shows the molar ratio between CH₄ and the sum of all detectable carbon-based gases, i.e., CH₄, CO and CO₂ ($\frac{CH_4}{CH_4+CO+CO_2}$) and the reactivity of iron sand over 10 methane pulses for a fully oxidized iron sand and 10 pulses for a partially reduced iron sand in logarithmic form. Every point represents one pulse.

The molar ratio of CH₄ to the total carbon (CH₄ + CO + CO₂) represents the fraction of unconverted methane over the investigated mass conversion degrees. The graph shows a high fraction of unconverted methane even from the beginning, ranging from 0.8 to 0.93 depending on the temperature. This might indicate that iron sand is not that reactive toward methane, which is also the case with the well-known iron-ore-based oxygen carrier ilmenite [38]. The percentage of unconverted methane rapidly increased toward almost 100 % as iron sand was reduced further, yet this number is still higher at 850 °C compared with that at 950 °C. This clearly demonstrated that methane conversion is more enhanced at higher temperatures. At the same time, iron sand's reactivity went down. This is reasonable as more unconverted CH₄ indicates a decrease in the available oxygen, which in turn gives a lower reactivity. Here it can also be seen that the reactivity of iron sand was higher at higher temperatures. The reactivity decreased rapidly during the first stage of reduction and eventually stabilized at higher reduction degrees of the material. The reactivity at the highest temperature, 950 °C, did not decline as fast for the lower temperatures. Nonetheless, the rapid increase in the fraction of unconverted methane and rapid decrease in iron sand's reactivity show that iron sand might only be able to carry a limited amount of oxygen. At this stage, nearly all the available oxygen may have been exhausted, possibly leading to the formation of wüstite or elemental iron, see sub-section 3.3.1. The data at 850 and 875 °C suggest that the oxygen transfer capacity of iron sand toward methane (R_{O,CH_4}) is slightly lower than 1 wt%, while those at higher temperatures still show some fuel conversion and therefore cannot be used as a basis to calculate R_{O,CH_4} . These findings suggest that iron sand is a suitable candidate for a chemical-looping process that requires less oxygen, such as CLG or chemical-looping reforming (CLR), where partial

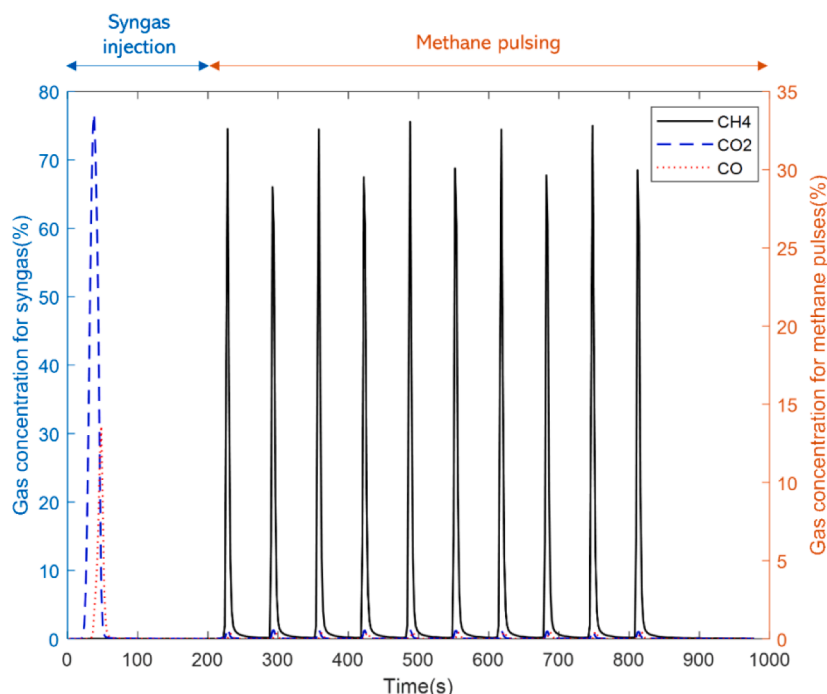


Fig. 3. Concentration profile of a 30-second syngas injection (left) followed by the pulsing of methane (right) at 900 °C.

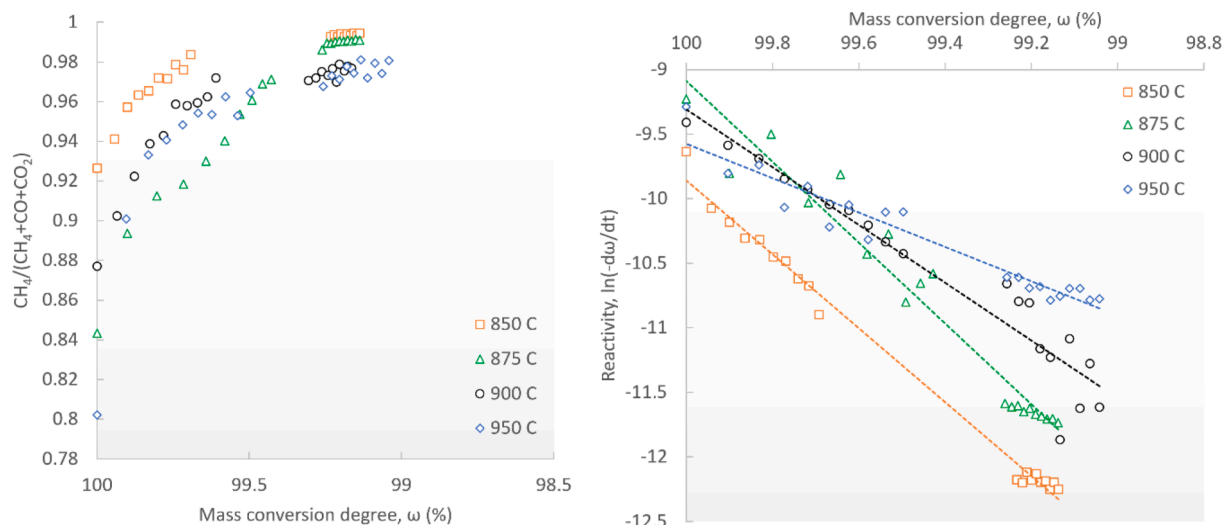


Fig. 4. The molar ratio of CH_4 to the sum of CH_4 , CO and CO_2 (left) and reactivity, in logarithmic form (right) of iron sand toward methane as functions of mass conversion degree.

oxidation of fuels is expected to take place.

3.1.2. Investigations using carbon monoxide

Iron-based oxygen carriers are known to have a higher reactivity toward carbon monoxide (CO) compared to methane. Therefore, here the oxygen carrier bed is a mixture of iron sand and quartz sand, with the latter being unable to undergo reduction – oxidation reaction. Similar to the experiment with methane, the oxygen carrier bed containing was first reduced with syngas before CO pulsing. Fully oxidized oxygen carrier bed was also examined with CO pulses for the sake of comparison. Mass conversion degrees of iron sand set by pre-reduction with syngas prior to the CO pulsing can be seen in Table S.2.

During the experiment, there were barely any changes in the mass conversion degree when iron sand was reduced by more than 60 s. This demonstrates a limitation of the available oxygen capacity of iron sand. Defluidization of the oxygen carrier bed did occur when syngas was injected for more than 40 s at 950 and 975 °C, yet no apparent agglomeration was observed when the sample was taken out from the reactor. The defluidization at 950 °C was temporary and could be solved

by cooling down the system and heating it up again, while the defluidization happened at 975 °C remained even after cooling down and reheating. A previous study reported that the combination of highly reducing environment and high temperature has indeed caused defluidization in iron-based oxygen carrier bed, particularly toward highly reactive gaseous fuel such as syngas, or CO in this case, due to the formation of wüstite or elemental iron [3]. Both these phases were observed in the XRD of a highly reduced iron sand sample which will be explained later in sub-section 3.3.1. The fact that no agglomerates were observed in the cooled-down sample did not necessarily imply the absence of agglomeration at reaction temperatures; however, it was not possible to confirm the relevant mechanism behind this. This particular defluidization should not be perceived as discouraging as iron sand was mixed with quartz sand in this case; thus, the defluidization may not necessarily represent the fluidization performance of the iron sand itself.

Fig. 5 shows the molar ratio of outlet CO, which was the gaseous fuel, to the sum of CO and CO_2 , and the reactivity of iron sand in logarithmic form, which was calculated according to Equation (5). It can be clearly seen that CO increased as the mass conversion degree decreased as a

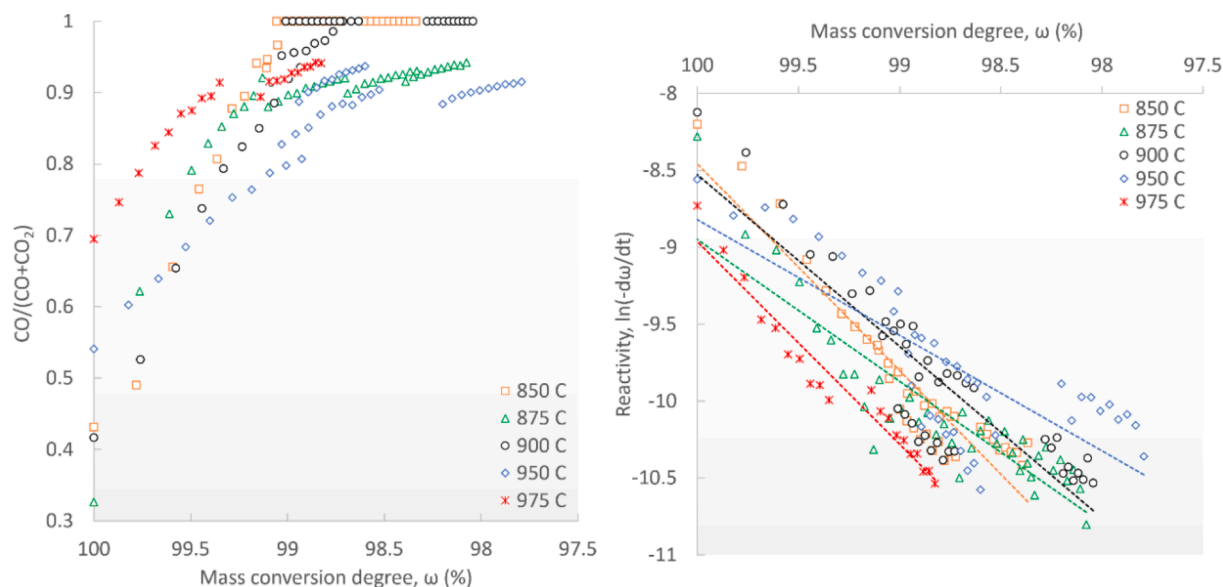


Fig. 5. The molar ratio of CO to the sum of CO and CO_2 (left) and the reactivity, in logarithmic form (right) of iron sand toward carbon monoxide as functions of mass conversion degree. All pulses are included in these graphs.

function of the number of pulses. Eventually, only unconverted CO was present in the bed and, subsequently, no more CO₂ was produced, which indicated that there was no more available oxygen in the oxygen carrier. The data at 850 and 900 °C indicate that the oxygen transfer capacity of iron sand toward CO ($R_{O,CO}$) is slightly higher than 1 wt%. The data at the other temperatures cannot be used to determine the oxygen transfer capacity since the conversion of CO was still occurring during the end of experiments. At the same time, the reactivity of iron sand toward CO declined as the mass conversion degree decreased. Compared to the reactivity toward methane, iron sand showed a much higher reactivity toward CO and a slower declining trend, which was expected. However, the graph shows that the reactivity does not differ much between temperatures, even for the fully oxidized iron sand. The fact that the reactivity at the highest temperature, 975 °C, was the lowest amongst all could be caused by the defluidization taking place at this temperature. The fluidization behavior of iron sand is elaborated in section 3.4.

3.2. Solid fuel conversion of pine forest char using iron sand

3.2.1. The effect of mass conversion degree on H₂ and CO concentrations

Iron sand was used in the conversion of pine forest residue at four temperatures and multiple mass conversion degrees. The values of mass conversion degrees set by pre-reduction with diluted CO prior to the solid fuel conversion can be seen in Table S.3.

Fig. 6 shows the average hydrogen partial pressure in the bed and the molar ratio of CO to the sum of CO and CO₂ as functions of mass conversion degree (ω) of the oxygen carrier for the solid fuel experiments.

It can be seen that the presence of both hydrogen and CO in the particle bed generally became higher as iron sand was reduced further. These increasing trends were expected as the available oxygen in the iron sand bed became lower and, therefore, the conversion of CO and H₂ to CO₂ and H₂O, respectively, became less favorable. From these data, the partial pressure of oxygen in the bed can be determined and used as the basis for thermodynamic calculations in sub-section 3.3.2. Based on the data at 950 and 975 °C, the amount of CO and H₂ generated from the conversion of pine forest residue char using iron sand at mass conversion degrees of around 99 wt% is at a comparable level with that using ilmenite at mass conversion degrees of around 97 wt% [23]. This suggests that the use of iron sand as an oxygen carrier is likely more preferred than ilmenite if the main aim is to generate syngas like in CLG.

3.2.2. Char reactivity toward iron sand

In order to calculate the rate constants and activation energy of the char toward iron sand, an Arrhenius plot was made according to

Equation (10) and is shown in Fig. 7. The reaction rate was calculated according to Equation (7) as an average from three repeated cycles, with a standard deviation value between 0.0002 and 0.001. The mass conversion degrees of iron sand shown in the figure are the average of the values shown in Table S.3 taken for the same duration of CO injection. The corresponding rate constants and activation energy values are shown in Table 6.

Based on Table 6, the char conversion rate constant decreased as iron sand was reduced even further. At the same time, the activation energy also decreased, despite not significantly. It has been known that the atmosphere in the bed can influence the activation energy of char conversion [39]. In this case, the mass conversion degree of iron sand affected the gaseous phase atmosphere, e.g., H₂ concentration. The activation energy of the conversion of pine forest residue char using iron sand as the oxygen carrier are slightly lower than that when using ilmenite [23]. This suggests that iron sand can be utilized as the oxygen carrier in a biomass char conversion.

A slower char conversion rate could be caused by both hydrogen and CO inhibition [32,33]. As explained above in section 2.6, the effect of hydrogen inhibition was expected to be more relevant compared to that of CO inhibition in this study [34]. To examine the effect of increasing hydrogen partial pressure on the pine forest residue (Table 7) char conversion, the corresponding conversion rate was plotted against the average hydrogen partial pressure in Fig. 8. Furthermore, as explained earlier, the LHHW models were deemed suitable to determine the relevant mechanisms that may have caused the hydrogen inhibition effect in this study, which involved a steam char conversion. To obtain the corresponding parameters mathematically based on Equation (12) and (13), the inverse fraction of the conversion rate was plotted as a function of average hydrogen partial pressure, or the square root of hydrogen partial pressure for the DHA model. The obtained parameters are provided in Table 7.

In Fig. 8, it can be seen that a higher hydrogen level led to a slower char conversion rate at 950 and 975 °C, which is likely explained by hydrogen inhibition [40]. However, the trend at 850 and 900 °C are inconclusive. With respect to the model validation, the OE/AHA models fit better with the experimental data due to a negative parameter in the DHA model, which is not realistic. This implies that either oxygen exchange or associative hydrogen adsorption mechanism discussed by Azimi et al. [30] may have possibly taken place in the conversion of pine forest residue using iron sand. Given that the proposed mechanisms are all based on surface reactions and both mechanisms shared the same rate formula, it is challenging to determine which among the mechanisms was the one that did occur. Nonetheless, a previous study by Lussier

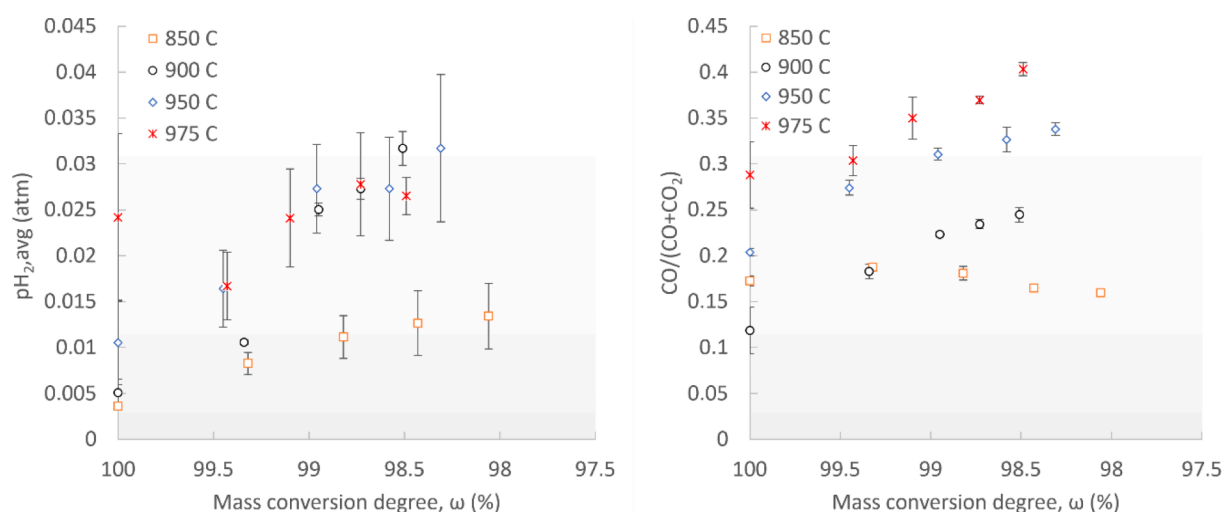


Fig. 6. The average hydrogen partial pressure (left) and the molar ratio of CO to the sum of CO and CO₂ (right) as functions of mass conversion degree of iron sand using pine forest residue char.

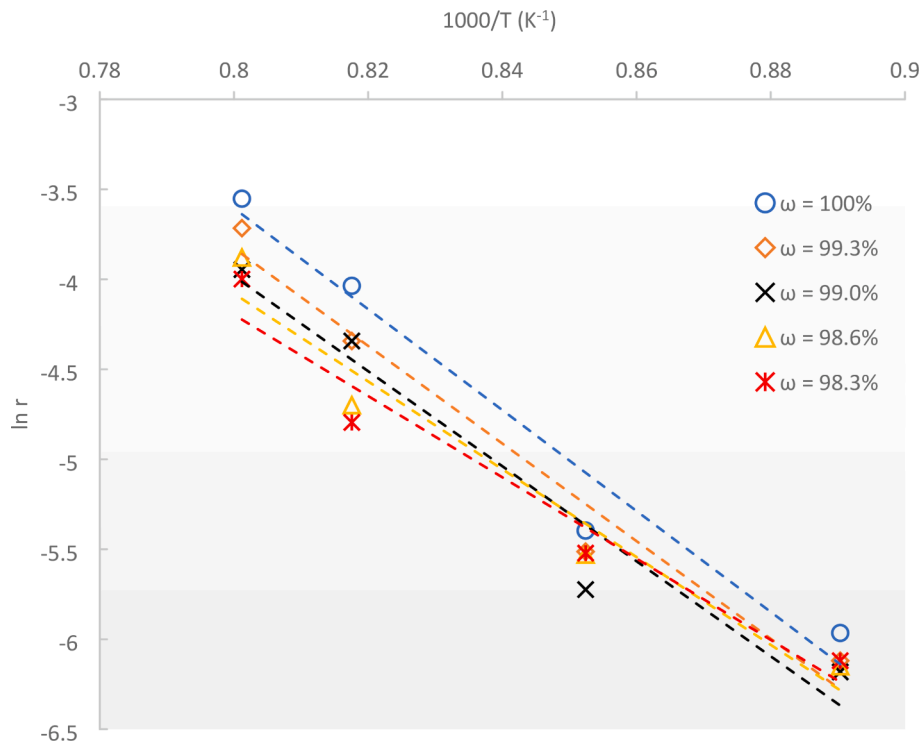


Fig. 7. The Arrhenius plot for the conversion of pine forest residue char with iron sand as oxygen carrier.

Table 6

The rate constants and activation energy for the conversion of pine forest residue char with iron sand as oxygen carrier.

Parameter	Mass conversion degree (ω), in %				
	100	99.3	99.0	98.6	98.3
k (s ⁻¹)	1.49×10^8	5.75×10^7	2.78×10^7	5.06×10^6	1.05×10^6
E _a (kJ/mol)	234	225	219	203	187

Table 7

The obtained parameters for three Langmuir-Hinshelwood/Hougen-Watson mechanism models.

Model	Rate expression and unit	Parameters			
		850 °C	900 °C	950 °C	975 °C
OE/AHA	$r = \frac{1}{a + b p H_2} a$ in s, b in s.atm ⁻¹	a = 369 b = 8,215	a = 222 b = 1,630	a = 28 b = 2,813	a = 26 b = 794
DHA	$r = \frac{1}{a + b \sqrt{p H_2}} a$ in s, b in s.atm ^{-0.5}	a = 304 b = 1,497	a = 195 b = 440	a = -25 b = 788	a = 10 b = 229

et al. [41] stated that the oxygen exchange mechanism was the most likely mechanism taking place in a char conversion at temperatures above 727 °C since all adsorbable hydrogen has been exhausted at lower temperatures.

Overall, this demonstrates that iron sand was able to convert solid fuels into gaseous products well. The conversion of pine forest residue using ilmenite also showed a similar reactivity to that using iron sand in this study [23]. Even at lower mass conversion degrees (ω less than 98.5 wt%), the $(\frac{CO}{CO+CO_2})$ ratios were still less than 0.5, which indicates the conversion of solid fuel to CO₂ was still reasonable, see Fig. 6. It should also be noted that the mass conversion degree of iron sand had an indirect effect in enhancing the hydrogen inhibition effect, which in turn gave a slower conversion rate of pine forest residue char.

3.3. Characterization of iron sand

3.3.1. Crystalline phases of iron sand

Fig. 9 shows the diffractogram of iron sand at different mass conversion degrees from a separate experiment, which was explained in section 2.7. The corresponding phases are provided in Table 8.

In the fresh fully oxidized iron sand, both hematite and magnetite were present, with the former having higher intensity than the latter in the diffractogram. The intensity of hematite decreased as the iron sand was reduced, while that of magnetite became more dominant. Silicon oxide (SiO₂) was detected in the fully oxidized iron sand in two different phases, cristobalite and quartz. The latter phase was not present in the used oxidized sample, this could be due to the fact that cristobalite is more stable than quartz. Furthermore, cristobalite was still detected in the reduced samples, but quartz was no longer found at all in the reduced iron sand samples. In these samples, the phases of iron silicon oxide, including fayalite, were formed. This suggested that quartz reacted with iron to form iron silicon oxide phases.[42] The phase transformation prediction by FactSage 8.1 also showed that quartz is not stable at temperatures higher than nearly 868 °C. The formation of elemental iron and wüstite at the highest degree of reduction indicated that iron sand at this stage had lost a substantial amount of available oxygen. Furthermore, one defludization phenomenon taking place during the investigations with CO might have been caused by the formation of these phases [3]. It should be noted that the elemental iron might have formed in a rather low amount. Despite the high reduction degree, a minor amount of hematite could still even be seen at the highest degree of reduction.

3.3.2. Thermodynamic study

The phase transition of iron sand during pine forest residue char conversion was studied using FactSage 8.1. The effect of temperature and oxygen partial pressure on the phase transformation was investigated. The oxygen partial pressure correlates to the conversion of CO to CO₂. Oxygen partial pressures were calculated using the equilibrium constant, determined by the reaction module, along with the measured

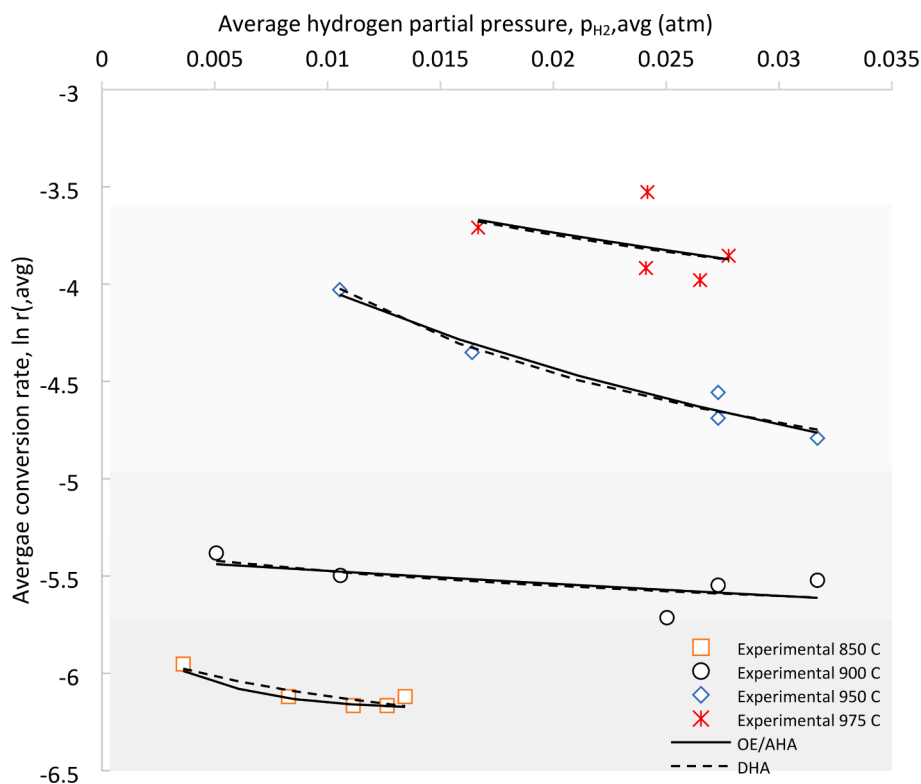


Fig. 8. Char conversion rate plotted, in logarithmic scale, as a function of hydrogen partial pressure. The validation of three LHHW models toward the experimental results is also included.

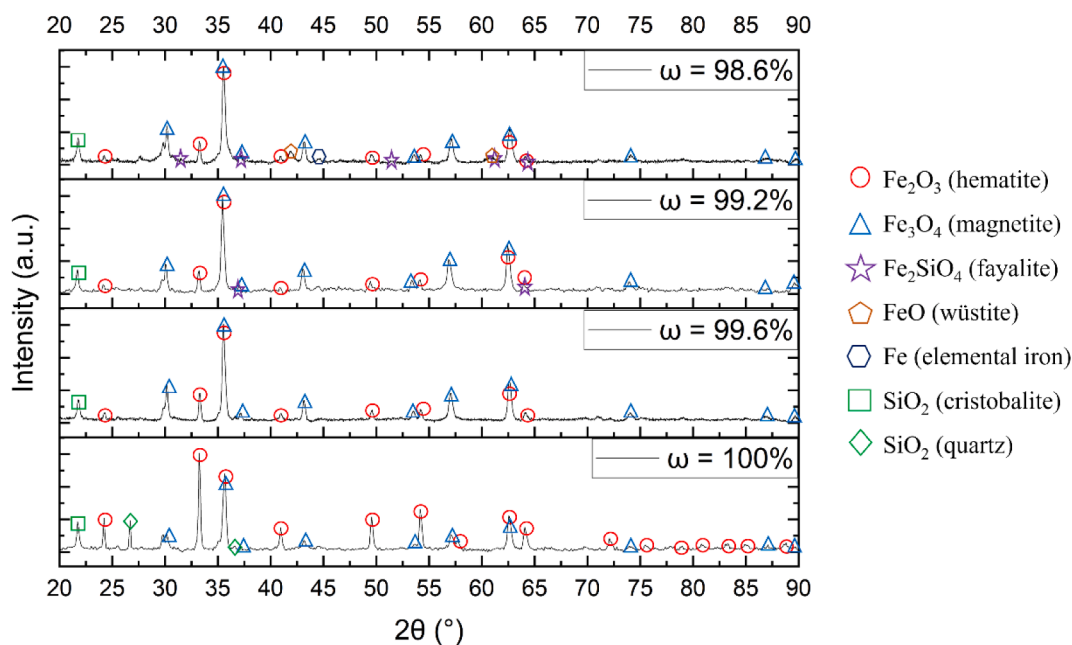


Fig. 9. The diffractogram of iron sand at mass conversion degrees taken after experiments with pure CO at 850 °C.

CO/(CO + CO₂) ratios from Fig. 6. The triangles in the diagram illustrate the expected phases after each experiment. The circles illustrate phases where oxidation occurs (5 vol% O₂ in N₂). The phase diagram for iron sand over a temperature span and oxygen partial pressures is presented in Fig. 10.

The most oxidized form of iron sand is Fe₂O₃ and SiO₂, according to thermodynamic predictions. The crystalline phases determined by XRD confirmed the presence of both phases in the fully oxidized sample, see

Fig. 9 and Table 8. The oxygen-bearing phases according to thermodynamic predictions is as expected, provided by iron. The phase transformations that occur starting from the most oxidized form are Fe₂O₃ to spinel (Fe₃O₄) to Fe₂SiO₄ and lastly Fe. SiO₂ is present in all steps. Cristobalite is not included in the phase diagram as it does not form at temperatures below 1,460 °C. However, cristobalite was found in the heat-treated material. Iron sand is a by-product from copper smelting industry, which explains why cristobalite was detected in the iron sand

Table 8

The crystalline phases of iron sand at different reduction degrees.

Mass conversion degree (wt %)	Major phases	Minor phases	Trace phases
100	Fe ₂ O ₃ (hematite) SiO ₂ (cristobalite)	Fe ₃ O ₄ (magnetite) SiO ₂ (quartz)	–
99.6	Fe ₃ O ₄ (magnetite) SiO ₂ (cristobalite)	Fe ₂ O ₃ (hematite)	Fe _{3-x} Si _x O ₄ (iron silicon oxide)
99.2	Fe ₃ O ₄ (magnetite) SiO ₂ (cristobalite)	Fe ₂ O ₃ (hematite)	Fe ₂ SiO ₄ (fayalite)
98.6	Fe ₃ O ₄ (magnetite) FeO (wüstite) SiO ₂ (cristobalite)	Fe ₂ O ₃ (hematite)	Fe ₂ SiO ₄ (fayalite) Fe (elemental iron)

sample, see Table 8. In Fig. 10 it can be observed that the experiments are located close to the phase transition between Fe₂SiO₄ and Fe. Compared with the phases detected by XRD, the presence of magnetite (Fe₃O₄) and cristobalite (SiO₂) was confirmed in all stages of reduced iron sand samples. Wüstite (FeO) was detected by XRD but not predicted by FactSage. This is because the presence of Si prohibits the formation of FeO, since Fe₂SiO₄ is stable in the same region. During redox-reactions iron will form a layer on the particles, as shown in Fig. 12b in section 3.3.3. In areas where this separation of Fe has occurred, it is thermodynamically favored to form FeO during reduction. The thermodynamic calculations assume a perfect mixing of the elements. Thus, these layers create Fe-rich areas pushing the equilibrium towards FeO instead. The influence of ash layers has been previously addressed by Stanić et al [43]. Additionally, despite having low intensity, the peak of elemental iron (Fe) was detected in minor amounts by XRD. This shows that the thermodynamic calculations by FactSage 8.1 are aligned with the crystalline phases confirmed by XRD.

3.3.3. Surface morphology and elemental distribution of iron sand

To investigate how iron sand transformed throughout the experiment, particularly with respect to the experiments using pine forest residue char, the surface morphology of and elemental distribution in iron sand particles were examined using SEM and EDX, respectively. An exposure to multiple redox cycles may compromise physical and chemical properties of an oxygen carrier [44], hence performing this analysis on iron sand is important. Fig. 11 compares the SEM imaging for iron sand before and after the experiment with pine forest residue char.

The particles of fresh unused iron sand, in a fully oxidized state, had pointy edges and did not have any cracks on their surface. The shape of many particles was rather long instead of round. After being exposed to the investigations with pine forest residue char, some fine fragments were formed, which could be a mix between the eroded iron sand particles and the ash from pine forest residue char. Despite having a somewhat rougher surface, the particles still had pointy edges and did not seem to have been significantly worn down. This can be an indication that iron sand might have good durability when used in fluidized bed applications; however, more studies will be needed to confirm this.

Fig. 12 shows the elemental distribution in iron sand particles seen under EDX analysis, both before and after the experiment with pine forest residue char. The experiment was performed at four temperatures (850, 900, 950, 975 °C) for a total of 60 oxidation – reduction cycles with a total inserted amount of pine forest residue char of 6 g. The conditions can be seen in Table 4.

Before the experiments with pine forest residue char, in general, all elements were distributed quite evenly within every particle. The exception was calcium that was present mostly on the particles' surface. There was also a single particle that only contained SiO₂, which could be assumed to be a pure sand particle. After the experiments, ash elements were also detected in the particle bed. Fig. 12b shows an ash particle and an iron sand particle on the left and right sides, respectively. The elements detected in the ash were mainly silicon and calcium. Iron seemed to form a layer on the iron sand particle's surface, which suggested that iron would migrate to the outer layer during highly reducing environments where it most likely formed wüstite [45]. A similar outward migration of iron was also seen in a sample investigated with gaseous

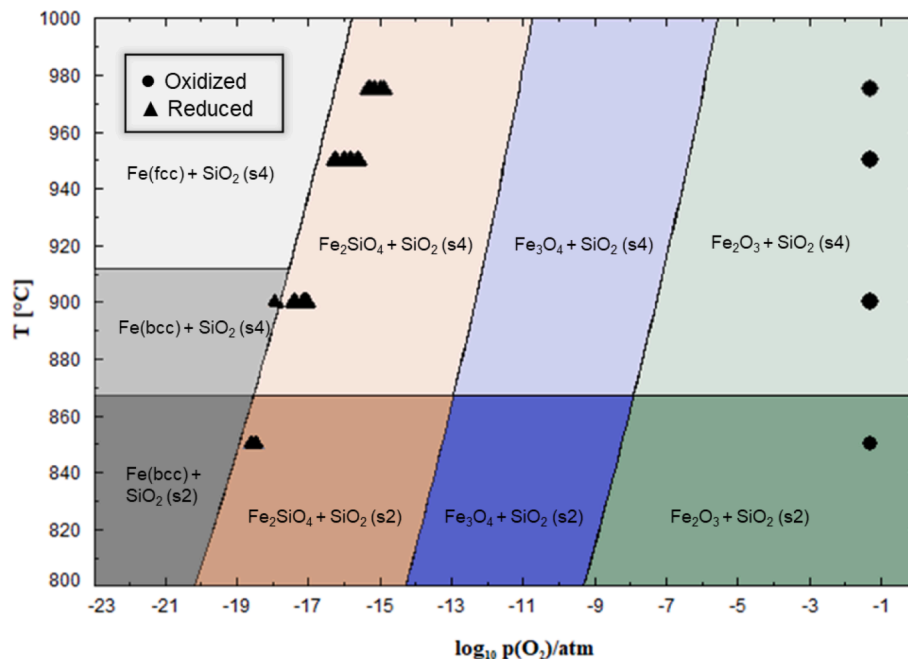


Fig. 10. The phase diagram for iron sand over relevant temperatures and oxygen partial pressures for fluidized bed gasification. Calculations were performed at 1 atm using Fe: Si weight ratio 35:16. Quartz is denoted by (s2) and tridymite by (s4). The circles indicate the point for oxidation and the triangles indicate the expected positions for the experimental measurements.

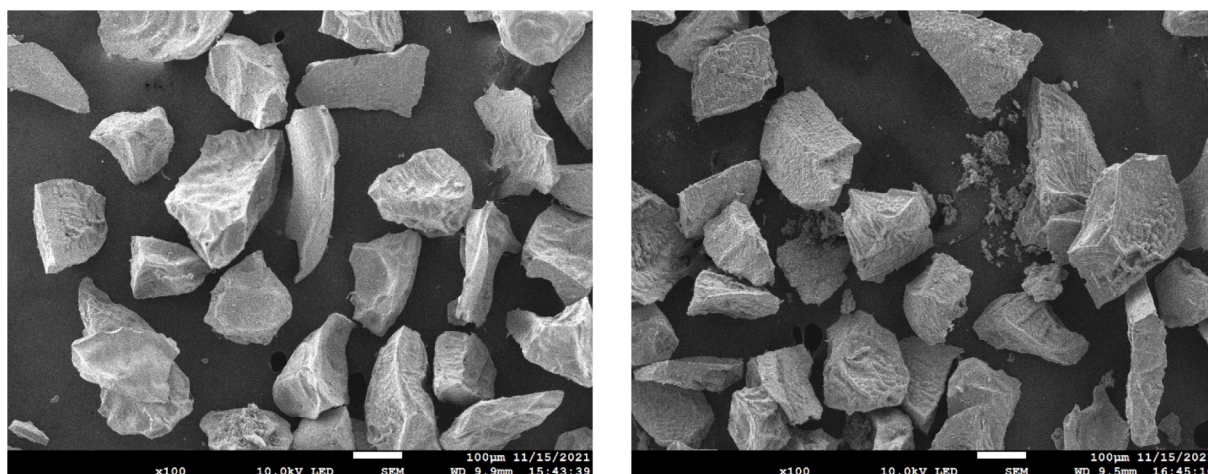
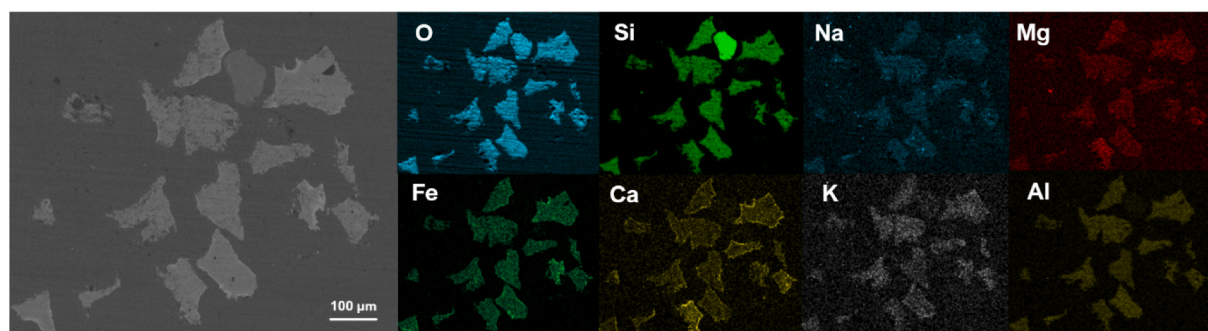
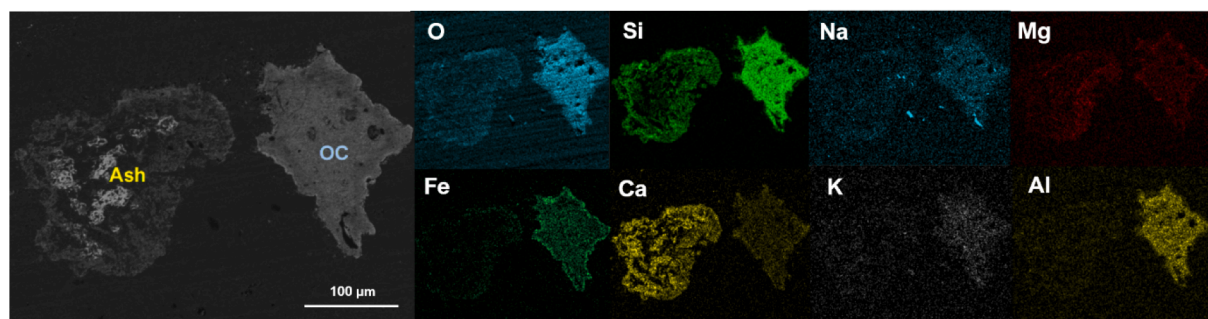


Fig. 11. The SEM images of iron sand before (left) and after (right) experiment with pine forest residue char. Iron sand in fully oxidized (before) and reduced (right) state.



(a) Before



(b) After

Fig. 12. The elemental distribution in iron sand particles before and after experiment with solid fuels. The experiment was performed at four temperatures (850, 900, 950, 975 °C) for a total of 60 oxidation – reduction cycles with a total inserted amount of pine forest residue char of 6 g.

fuels. Silicon oxide seemed to make up a large portion of the particle core, but some iron was also detected in the core. This could explain the formation of the iron silicon oxide phases confirmed by XRD. Additionally, silica is believed to be the element that bound the alkali elements into the particle [46]. Therefore, it is not strange that trace amounts of calcium, sodium, potassium and magnesium were detected within the particle. Aluminum, however, seemed to be almost completely enclosed within the particle and was not present at all in the ash layer. Due to the low aluminum content in the fuel, this was most likely the aluminum that was already present as a contaminant in the fresh oxygen carrier bulk, see Table 1. These are the first findings

reported for ash interactions with iron sand used for chemical looping processes. More research is needed to investigate the behavior and interaction with different fuels. Nevertheless, the fact that no agglomerations or melts were detected in this study is promising for fluidized bed applications.

3.4. Fluidization performance of iron sand at high reduction degrees

Both experiments using the gaseous fuels CH_4 and CO indicate that the oxygen transfer capacity of iron sand, about 1 wt%, is clearly lower than ilmenite, a benchmark oxygen carrier with an oxygen transfer

capacity of 5 wt% [11]. This is in line with the fact that the conversion of the gaseous fuels to CO₂ using iron sand is clearly lower than that using ilmenite [11]. Hence, a reduction by 1 wt% might be considered low for ilmenite but rather high for iron sand. Instead of being a disadvantage, this limitation can in turn be useful to establish partial oxidation of fuel, which may take place in chemical looping gasification or reforming, provided the material does not show major fluidization issues. With respect to limiting the oxygen transfer from AR to FR in such processes, a lower oxygen transfer capacity of the oxygen carrier is a natural advantage.

Ilmenite did defluidize when reduced by around 3 – 4 wt% and phases like FeO started to form [3]. Yet iron sand did not defluidize despite being highly reduced by around 1 wt%, where FeO might have started to form, using both CH₄ and CO. As discussed above, the defluidization of iron sand in the experimental series using CO at 950 and 975 °C should not be taken into account when evaluating the fluidization performance of iron sand itself as the material was mixed with quartz sand in this case. It should also be noted that the superficial velocities in the batch reactor were rather low, i.e., between 0.07 and 0.19 m/s, depending upon the fluidizing gases and temperatures. This is considerably lower than what one would expect in a real fluidized bed system, where the fluidization flows are on the order of, for example, 1 – 10 m/s in a 100-kW chemical looping unit, depending upon the fluidization regime [47]. Furthermore, the material did not defluidize at all during the experiments using the solid fuel pine forest residue char even at higher reduction degrees. Therefore, it can be concluded that the fluidization performance of iron sand is acceptable.

4. Conclusion

Iron sand, a by-product of the copper smelting process, can be utilized as an oxygen carrier in chemical looping processes, especially the ones requiring low oxygen demand like CLG. The major advantage is that this iron sand is generated in significant quantities as an offshoot in size ranges that are applicable for chemical-looping processes, thus requiring a very low cost. Our findings can be elaborated as follows:

- Based on the investigations using the gaseous fuels CH₄ and CO, the oxygen transfer capacity of iron sand was found to be 1 wt%, which is much lower than that of ilmenite. This suggests that iron sand is likely a suitable oxygen carrier candidate if the aim of the process is to generate syngas, such as in CLG.
- The kinetics of pine forest residue char conversion using iron sand likely followed the oxygen exchange mechanism, which was modeled according to the Langmuir-Hinshelwood models. Depending on the mass conversion degree of iron sand, the activation energy of pine forest residue conversion was between 187 and 234 kJ/mol, which is slightly lower than that of ilmenite. This is obviously an advantage since one prefers a lower activation energy in any reaction.
- The generation of CO and H₂ from pine forest residue char using 1 wt %-reduced iron sand was at a comparable level with that using a 3 wt %-reduced ilmenite, especially at 950 and 975 °C. Once again, this suggests the advantage of using iron sand as an oxygen carrier in CLG to generate syngas as the material does not need to be reduced as further as ilmenite to generate the same amount of hydrogen.
- The fluidization performance of iron sand was acceptable, i.e., no defluidization of the bed containing only iron sand occurred even at higher reduction degrees (ω = 98 – 99 wt%). This implies that the material will likely not suffer from a major fluidization problem when used in CLG, where a higher reduction degree of the material can be expected.
- The crystalline phase transformation in iron sand at multiple mass conversion degrees during reduction was predicted by thermodynamics and successfully confirmed by XRD. This is certainly a useful

scientific information of iron sand as an oxygen carrier that is exposed to multiple reduction – oxidation cycles.

Declaration of Competing Interest

The authors declare that they have no known competing financial interests or personal relationships that could have appeared to influence the work reported in this paper.

Data availability

Data will be made available on request.

Acknowledgments

The authors acknowledge the Swedish Energy Agency for funding this project (Project 51430-1). Boliden AB is acknowledged for valuable input and providing for the iron sand material. The characterization work was performed at the Chalmers Material Analysis Laboratory (CMAL). The authors appreciate Daniel Brantebäck and Joel Amrén for performing parts of the experimental work in this study and Fredrik Hildor for his assistance in BET surface area measurements.

Appendix A. Supplementary data

Supplementary data to this article can be found online at <https://doi.org/10.1016/j.fuel.2022.127310>.

References

- [1] K. Wang et al., "Understanding of the oxygen uncoupling characteristics of Cu-Fe composite oxygen carriers for chemical-looping gasification," *Fuel Process. Technol.*, vol. 218, no. April, 2021, 10.1016/j.fuproc.2021.106844.
- [2] M. Rydén et al., "Negative CO₂ Emissions with Chemical-Looping Combustion of Biomass - A Nordic Energy Research Flagship Project," *Energy Procedia*, vol. 114, no. November 2016, pp. 6074–6082, 2017, 10.1016/j.egypro.2017.03.1744.
- [3] V. Purnomo, D. Yilmaz, H. Leion, and T. Mattisson, "Study of defluidization of iron- and manganese-based oxygen carriers under highly reducing conditions in a lab-scale fluidized-bed batch reactor," *Fuel Process. Technol.*, vol. 219, no. December 2020, p. 106874, 2021, 10.1016/j.fuproc.2021.106874.
- [4] Wang X, et al. High-throughput oxygen chemical potential engineering of perovskite oxides for chemical looping applications. *Energy Environ Sci* 2022;15 (4):1512–28. <https://doi.org/10.1039/d1ee02889h>.
- [5] Qasim M, Ayoub M, Ghazali NA, Aqsha A, Ameen M. Recent Advances and Development of Various Oxygen Carriers for the Chemical Looping Combustion Process: A Review. *Ind Eng Chem Res* 2021;60(24):8621–41. <https://doi.org/10.1021/acs.iecr.1c01111>.
- [6] Yilmaz D, Steenari BM, Leion H. Comparative Study: Impacts of Ca and Mg Salts on Iron Oxygen Carriers in Chemical Looping Combustion of Biomass. *ACS Omega* 2021. <https://doi.org/10.1021/acsomega.1c02138>.
- [7] Y. De Vos, M. Jacobs, P. Van Der Voort, I. Van Driessche, F. Snijsers, and A. Verberckmoes, "Development of stable oxygen carrier materials for chemical looping processes—A review," *Catalysts*, vol. 10, no. 8, 2020, 10.3390/catal10080926.
- [8] Sikarwar SS, Vooradi R, Patnaikuni VS, Kakunuri M, Surywanshi GD. A novel thermally stable Fe₂O₃/Al₂O₃ nanofiber-based oxygen carrier for chemical-looping combustion. *Chem Pap* 2022;76(6):3987–93. <https://doi.org/10.1007/s11696-022-02129-9>.
- [9] Yu Z, et al. Iron-based oxygen carriers in chemical looping conversions: A review. *Carbon Resour Convers* 2019;2(1):23–34. <https://doi.org/10.1016/j.crcon.2018.11.004>.
- [10] Matzen M, Pinkerton J, Wang X, Demirel Y. Use of natural ores as oxygen carriers in chemical looping combustion: A review. *Int J Greenh Gas Control* 2017;65:1–14. <https://doi.org/10.1016/j.ijggc.2017.08.008>.
- [11] Leion H, Lyngfelt A, Johansson M, Jerndal E, Mattisson T. The use of ilmenite as an oxygen carrier in chemical-looping combustion. *Chem Eng Res Des* 2008;86(9): 1017–26. <https://doi.org/10.1016/j.cherd.2008.03.019>.
- [12] Pissot S, Berdugo Vilches T, Maric J, Cañete Vela I, Thunman H, Seemann M. Thermochemical Recycling of Automotive Shredder Residue by Chemical-Looping Gasification Using the Generated Ash as Oxygen Carrier. *Energy Fuel* 2019;33(11): 11552–66. <https://doi.org/10.1021/acs.energyfuels.9b02607>.
- [13] Moldenhauer P, Rydén M, Lyngfelt A. Testing of minerals and industrial by-products as oxygen carriers for chemical-looping combustion in a circulating fluidized-bed 300 W laboratory reactor. *Fuel* 2012;93:351–63. <https://doi.org/10.1016/j.fuel.2011.11.009>.

- [14] Deng G, et al. Enhanced performance of red mud-based oxygen carriers by CuO for chemical looping combustion of methane. *Appl Energy* 2019;vol. 253, no. February:113534. <https://doi.org/10.1016/j.apenergy.2019.113534>.
- [15] Mendiara T, de Diego LF, García-Labiano F, Gayán P, Abad A, Adánez J. Behaviour of a bauxite waste material as oxygen carrier in a 500Wth CLC unit with coal. *Int J Greenh Gas Control* 2013;17:170–82. <https://doi.org/10.1016/j.ijggc.2013.04.020>.
- [16] Chen L, Zhang Y, Liu F, Liu K. Development of a cost-effective oxygen carrier from red mud for coal-fueled chemical-looping combustion. *Energy Fuel* 2015;29(1): 305–13. <https://doi.org/10.1021/ef501950w>.
- [17] F. Störmer, F. Lind, and M. Rydén, “Oxygen carrier aided combustion in fluidized bed boilers in Sweden—review and future outlook with respect to affordable bed materials,” *Appl. Sci.*, vol. 11, no. 17, 2021, 10.3390/app11177935.
- [18] Alp I, Deveci H, Süngün H. Utilization of flotation wastes of copper slag as raw material in cement production. *J Hazard Mater* 2008;159(2–3):390–5. <https://doi.org/10.1016/j.jhazmat.2008.02.056>.
- [19] Condori O, de Diego LF, García-Labiano F, Izquierdo MT, Abad A, Adánez J. Syngas production in a 1.5 kWth biomass chemical looping gasification unit using Fe and Mn ores as the oxygen carrier. *Energy Fuel* 2021;35(21):17182–96. <https://doi.org/10.1021/acs.energyfuels.1c01878>.
- [20] J. Leveneur et al., “Ironsand (Titanomagnetite-titanohematite): Chemistry, magnetic properties and direct applications for wireless power transfer,” *Materials (Basel)*, vol. 14, no. 18, pp. 5455 (1–15), 2021, 10.3390/ma14185455.
- [21] Tani H, Inazumi T, Terashima K. Mineralogical study of iron sand with different metallurgical characteristic to smelting with use of Japanese classic ironmaking furnace ‘tatara’. *ISIJ Int* 2014;54(5):1044–50. <https://doi.org/10.2355/isijinternational.54.1044>.
- [22] Dong N, et al. Chemical looping gasification of sewage sludge using copper slag modified by NiO as an oxygen carrier. *Chinese J Chem Eng* 2021;29:335–43. <https://doi.org/10.1016/j.cjche.2020.09.007>.
- [23] Purnomo V, Mei D, Soleimanislim AH, Mattisson T, Leion H. Effect of the Mass Conversion Degree of an Oxygen Carrier on Char Conversion and Its Implication for Chemical Looping Gasification. *Energy Fuel* 2022;36(17):9768–79. <https://doi.org/10.1021/acs.energyfuels.2c00944>.
- [24] H. Leion, V. Frick, and F. Hildor, “Experimental method and setup for laboratory fluidized bed reactor testing,” *Energies*, vol. 11, no. 10, 2018, 10.3390/en1102505.
- [25] Feng Y, Yang Q, Zuo Z, Luo S, Ren D, Lin H. Study on Preparation of Oxygen Carrier Using Copper Slag as Precursor. *Front Energy Res* 2021;9(November):1–7. <https://doi.org/10.3389/fenrg.2021.781914>.
- [26] Schwebel GL, Sundqvist S, Krumm W, Leion H. Apparent kinetics derived from fluidized bed experiments for Norwegian ilmenite as oxygen carrier. *J Environ Chem Eng* 2014;2(2):1131–41. <https://doi.org/10.1016/j.jece.2014.04.013>.
- [27] P. Dieringer, F. Marx, F. Alobaid, J. Ströhle, and B. Eppe, “Process control strategies in chemical looping gasification-A novel process for the production of biofuels allowing for net negative CO₂ emissions,” *Appl. Sci.*, vol. 10, no. 12, 2020, 10.3390/app10124271.
- [28] Hildor F, Leion H, Linderholm CJ, Mattisson T. Steel converter slag as an oxygen carrier for chemical-looping gasification. *Fuel Process Technol* 2020;vol. 210, no. August:106576. <https://doi.org/10.1016/j.fuproc.2020.106576>.
- [29] Sundqvist S, Arjmand M, Mattisson T, Rydén M, Lyngfelt A. Screening of different manganese ores for chemical-looping combustion (CLC) and chemical-looping with oxygen uncoupling (CLOU). *Int J Greenh Gas Control* 2015;43:179–88. <https://doi.org/10.1016/j.ijggc.2015.10.027>.
- [30] Azimi G, Keller M, Mehdipoor A, Leion H. Experimental evaluation and modeling of steam gasification and hydrogen inhibition in Chemical-Looping Combustion with solid fuel. *Int J Greenh Gas Control* 2012;11:1–10. <https://doi.org/10.1016/j.ijggc.2012.07.018>.
- [31] Mei D, Soleimanislim AH, Lyngfelt A, Leion H, Linderholm C, Mattisson T. Modelling of gas conversion with an analytical reactor model for biomass chemical looping combustion (bio-CLC) of solid fuels. *Chem Eng J* 2021;no. November: 133563. <https://doi.org/10.1016/j.cej.2021.133563>.
- [32] Fushimi C, Wada T, Tsutsumi A. Inhibition of steam gasification of biomass char by hydrogen and tar. *Biomass Bioenergy* 2011;35(1):179–85. <https://doi.org/10.1016/j.biombioe.2010.08.017>.
- [33] Roberts DG, Harris DJ. High-pressure char gasification kinetics: CO inhibition of the C-CO₂ reaction. *Energy Fuel* 2012;26(1):176–84. <https://doi.org/10.1021/ef201174k>.
- [34] Zhang R, Wang QH, Luo ZY, Fang MX, Cen KF. Competition and Inhibition Effects during Coal Char Gasification in the Mixture of H₂O and CO₂. *Energy Fuel* 2013;27(9):5107–15. <https://doi.org/10.1021/ef4007998>.
- [35] Suranani S, Goli VR. Fuel Particle Size Effect on Performance of Fluidized Bed Combustor Firing Ground Nuts. *Int J Chem Eng Appl* 2012;3(2):147–51.
- [36] Hüttlinger KJ, Merdes WF. The carbon-steam reaction at elevated pressure: Formations of product gases and hydrogen inhibitions. *Carbon N Y* 1992;30(6): 883–94. [https://doi.org/10.1016/0008-6223\(92\)90011-K](https://doi.org/10.1016/0008-6223(92)90011-K).
- [37] Bale CW, et al. FactSage thermochemical software and databases, 2010–2016. *Calphad Comput Coupling Phase Diagrams Thermochem* 2016;54:35–53. <https://doi.org/10.1016/j.calphad.2016.05.002>.
- [38] Tan Y, Ridha FN, Duchesne MA, Lu DY, Hughes RW. Reduction Kinetics of Ilmenite Ore as an Oxygen Carrier for Pressurized Chemical Looping Combustion of Methane. *Energy Fuel* 2017;31(7):7598–605. <https://doi.org/10.1021/acs.energyfuels.7b01038>.
- [39] Saito T, Lin S. Coal Char Reaction with Oxygen Carrier in Chemical Looping Combustion. *Energy Fuel* 2019;33(8):7667–77. <https://doi.org/10.1021/acs.energyfuels.9b01017>.
- [40] Pineda DI, Chen JY. Modeling hydrogen inhibition in gasification surface reactions. *Int J Hydrogen Energy* 2015;40(18):6059–71. <https://doi.org/10.1016/j.ijhydene.2015.03.063>.
- [41] Lussier MG, Zhang Z, Miller DJ. Characterizing rate inhibition in steam/hydrogen gasification via analysis of adsorbed hydrogen. *Carbon N Y* 1998;36(9):1361–9. [https://doi.org/10.1016/S0008-6223\(98\)00123-7](https://doi.org/10.1016/S0008-6223(98)00123-7).
- [42] Morris RC, Fletcher AB. Increased solubility of quartz following ferrous-ferric iron reactions. *Nature* 1987;330(6148):558–61. <https://doi.org/10.1038/330558a0>.
- [43] Stanić I, Andersson V, Hanning M, Mattisson T, Backman R, Leion H. Combined manganese oxides as oxygen carriers for biomass combustion — Ash interactions. *Chem Eng Res Des* 2019;149:104–20. <https://doi.org/10.1016/j.cherd.2019.07.004>.
- [44] Cabello A, et al. Qualification of operating conditions to extend oxygen carrier utilization in the scaling up of chemical looping processes. *Chem Eng J* 2021;430 (September):2022. <https://doi.org/10.1016/j.cej.2021.132602>.
- [45] L. Guo, S. Zhong, Q. Bao, J. Gao, Z. Guo, “Nucleation and growth of iron whiskers during gaseous reduction of hematite iron ore fines,” *Metals (Basel)*, vol. 9, no. 7, 2019, doi: 10.3390/met9070750.
- [46] M. Rydén, M. Hanning, F. Lind, “Oxygen Carrier Aided Combustion (OCAC) of wood chips in a 12 MWth circulating fluidized bed boiler using steel converter slag as bed material,” *Appl. Sci.*, vol. 8, no. 12, 2018, 10.3390/app8122657.
- [47] Linderholm C, Schmitz M, Lyngfelt A. Estimating the solids circulation rate in a 100-kW chemical looping combustor. *Chem Eng Sci* 2017;171:351–9. <https://doi.org/10.1016/j.ces.2017.05.025>.